Physics of Fluids ARTICLE scitation.org/journal/phf

Integral measures of the zero pressure gradient boundary layer over the Reynolds number range $0 \le R_\tau < \infty$

Cite as: Phys. Fluids **33**, 085108 (2021); doi: 10.1063/5.0061535
Submitted: 27 June 2021 · Accepted: 20 July 2021 ·
Published Online: 4 August 2021

View Online Export Citation CrossMark

Brian J. Cantwell[a)]

AFFILIATIONS

Department of Aeronautics and Astronautics, Stanford University, Stanford, California 94305, USA

Note: This paper is part of the special topic, Tribute to Frank M. White on his 88th Anniversary.
[a)]**Author to whom correspondence should be addressed:** cantwell.brianj@gmail.com. **URL:** https://www.stanford.edu/~cantwell/

ABSTRACT

A recently developed mixing length model of the turbulent shearing stress has been shown to generate a universal velocity profile that provides an accurate approximation to incompressible pipe flow velocity profiles over a wide Reynolds number range [B. J. Cantwell, "A universal velocity profile for smooth wall pipe flow," J. Fluid Mech. **878**, 834–874 (2019)]. More recently, the same profile was shown to accurately approximate velocity profiles in channel flow, the zero pressure gradient boundary layer, and the boundary layer in an adverse pressure gradient [M. A. Subrahmanyam, B. J. Cantwell, and J. J. Alonso, "A universal velocity profile for turbulent wall flows," AIAA Paper No. 2021-0061, 2021 and M. A. Subrahmanyam, B. J. Cantwell, and J. J. Alonso, "A universal velocity profile for turbulent wall flows including adverse pressure gradient boundary layers," J. Fluid Mech. (unpublished) (2021)] The universal velocity profile is uniformly valid from the wall to the free stream at all Reynolds numbers from zero to infinity. At a low Reynolds number, the profile approaches the laminar channel/pipe flow limit. The primary measure of the Reynolds number used in this work is the friction Reynolds number $R_\tau = u_\tau \delta/\nu$. It is a little unusual to use R_τ for the boundary layer since it requires that the velocity profile be cutoff using an arbitrarily defined overall boundary layer thickness, δ. Because of the slow approach of the velocity to the free stream, different conventions used to define the thickness lead to different values of R_τ assigned to a given flow. It will be shown in this paper that, through its connection to channel/pipe flow, the universal velocity profile can be used to define a practically useful, unambiguous, measure of overall boundary layer thickness, called here the equivalent channel half height, δ_h. For $R_\tau > \approx 5000$, the universal velocity profile defines a Reynolds number independent shape function that can be used to generate explicit expressions for the infinite Reynolds number behavior of all the usual integral boundary layer measures; displacement thickness, momentum thickness, energy thickness, overall boundary layer thickness, and skin friction. The friction coefficient $C_f(R_{\delta_2})$ generated by the universal velocity profile accurately approximates data over a wide range of momentum thickness Reynolds numbers collected by Nagib *et al.* ["Can we ever rely on results from wall-bounded turbulent flows without direct measurements of wall shear stress?," AIAA Paper No. 2004-2392, 2004]. The universal velocity profile is used to integrate the von Kaŕmań boundary layer integral equation [T. von Kármán, "Uber laminaire und turbulente reibung," Z. Angew. Math. Mech. 1, 233–252 (1921)] in order to generate the various thicknesses and friction velocity as functions of the spatial Reynolds number, $R_x = u_e x/\nu$.

I. INTRODUCTION

The simplification of the incompressible Navier–Stokes equations in the early 1900s to the boundary layer approximation for high Reynolds number flow over a wall by Prandtl[6] and his students was one of the most important advances in the history of mechanics. However, at the time, only limited methods were available for solving the boundary layer equations that, though simpler than the Navier–Stokes equations, were still challenging because of their nonlinearity. So a number of simplified approaches were developed to produce approximate solutions suitable for estimating the drag of complex aerodynamic shapes such as airships and wings. These methods all used the von Karman[5] boundary layer integral Eq. (1) derived by integrating the boundary layer equations over the height of the boundary layer.

$$\frac{d\delta_2}{dx} + (2\delta_2 + \delta_1)\frac{1}{u_e}\frac{du_e}{dx} - \left(\frac{u_\tau}{u_e}\right)^2 = 0. \tag{1}$$

The function $u_e(x)$ is the free stream velocity and

$$u_\tau(x) \equiv \left(\frac{\tau_w}{\rho}\right)^{1/2}, \tag{2}$$

is called the friction velocity.

The displacement thickness is defined as

$$\delta_1(x) = \int_0^\delta \left(1 - \frac{u}{u_e}\right) dy. \tag{3}$$

The momentum thickness is

$$\delta_2(x) = \int_0^\delta \frac{u}{u_e}\left(1 - \frac{u}{u_e}\right) dy, \tag{4}$$

and, for completeness, the energy thickness is

$$\delta_3(x) = \int_0^\delta \frac{u}{u_e}\left(1 - \left(\frac{u}{u_e}\right)^2\right) dy, \tag{5}$$

where δ is a suitably defined boundary layer thickness. For laminar boundary layers, the most well known integral methods are due to Pohlhausen[7] and Thwaites.[8]

There are also a limited number of methods that integrate the Karman equation for turbulent boundary layers. One of the simplest to apply is the method due to Head.[9] He assumes the existence of two universal functions, F and G, for the turbulent boundary layer. The first function relates a modified boundary layer shape factor to the conventional shape factor, and the second relates the conventional shape factor to the entrainment velocity at the outer edge of the boundary layer. When these functions are combined with the friction law of Ludweig and Tillman,[10] all of the basic characteristics of the boundary layer can be determined. The main weakness is that the functions F and G are determined from experimental correlations that exhibit very limited universality. In the words of Head[9]

"*2.3. Determination of Functions F and G. For this purpose the experimental data of Newman and of Schubauer and Klebanoff have been used. In each case, values of δ were obtained from tables of the measured profiles, δ being arbitrarily defined as the value of y for which* $u/U = 0.995$. *From the values of δ and the corresponding values of* H, θ, U, *and x, the quantities* $(1/U)d/dx[U(\delta - \delta^*)]$ *and* $H_{\delta-\delta^*}$ *were obtained and are shown plotted in Fig. 1 and 2. If the assumptions made in the previous sections had been correct, and if both the analysis and the experimental data had been entirely free from error then, of course, the points obtained from the two sets of results should have coincided with common curves defining the two functions. In fact, however as will be seen from the Figures there is considerable scatter of the points, and in Fig. 1, there is a fairly marked and consistent discrepancy between the two sets of results, which makes the drawing of a hypothetical common curve, representing the function* $F(H_{\delta-\delta^*})$, *a somewhat arbitrary procedure.*"

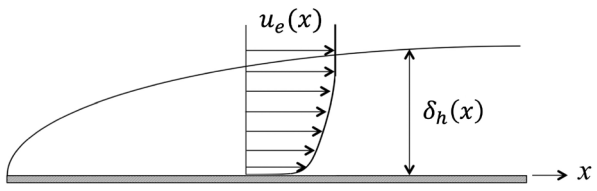

FIG. 1. Flat plate boundary layer notation.

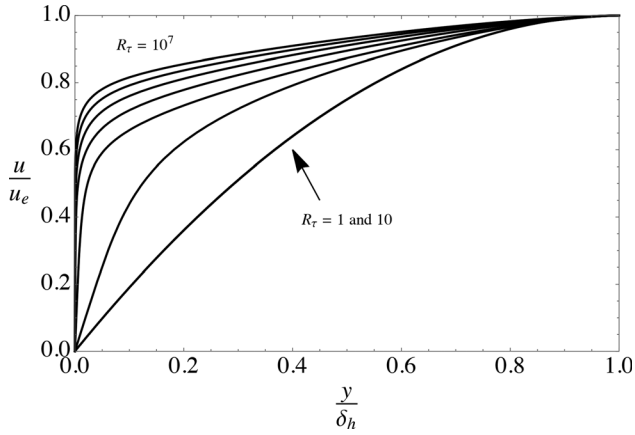

FIG. 2. The universal velocity profile at $R_\tau = 1, 10, 100, 1000, 10^4, 10^5, 10^6$, and 10^7.

II. BOUNDARY LAYER FLOW AND THE UNIVERSAL VELOCITY PROFILE

In this paper, a boundary layer integral method utilizing the universal velocity profile is used to generate the integral properties of the boundary layer on a wall. Zero, positive, and negative pressure gradient cases suggested in Fig. 1 can be addressed. However, in the present paper, we will restrict our attention to the zero pressure gradient case with a focus on the high Reynolds number limiting behavior of the flow.

At a high Reynolds number, the flow over a flat plate is accurately described by the boundary layer approximation (6)

$$\begin{gathered} 20\frac{\partial}{\partial x}(uu) + \frac{\partial}{\partial y}(uv) + \frac{\partial}{\partial y}(\overline{u'v'}) + \frac{1}{\rho}\frac{dp_e(x)}{dx} - \nu\frac{\partial^2 u}{\partial y^2} = 0, \\ \frac{\partial u}{\partial x} + \frac{\partial v}{\partial y} = 0, \end{gathered} \tag{6}$$

subject to the no-slip and free stream conditions

$$u(0) = v(0) = 0, \quad u(\delta_h) = u_e. \tag{7}$$

At Reynolds numbers large enough to produce turbulence, the no-slip condition imposed by viscosity leads to elongated three-dimensional convective motions near the wall that tend to align with the flow as a highly unsteady array of stream-wise eddies generating very strong convective and viscous wall-normal transport of x-momentum. The effect of this balance of viscous and convective stresses is to produce a well-defined wall layer with a very steep velocity gradient at the wall over a length scale comparable to the scale of the eddies just described. The mean velocity variation over this *viscous wall layer* scales with the friction velocity, Eq. (2). Most production of turbulent kinetic energy takes place within the wall layer. Above the wall layer, viscous stresses become small, and momentum

transport is dominated by turbulent eddying motions over a length scale comparable to the thickness of the boundary layer. The large scale eddies produce wall-normal convection of the turbulence generated at the wall leading to a changing velocity profile that can be compared to the growth and decay of the thickness and velocity deficit of a plane wake. The velocity changeover this outer layer scales with the aptly named defect velocity $(u_e - u_\tau)$.

A. The universal velocity profile

The universal velocity profile comes from the solution of the channel (or pipe) flow equation,

$$\frac{\partial}{\partial y}\overline{u'v'} + \frac{1}{\rho}\frac{dp_e(x)}{dx} - \nu\frac{\partial^2 u}{\partial y^2} = 0, \tag{8}$$

where the pressure gradient is a constant. Express Eq. (8) in wall normalized coordinates.

$$y^+ = \frac{yu_\tau}{\nu} \quad u^+ = \frac{u}{u_\tau} \quad \tau^+ = -\frac{\overline{u'v'}}{{u_\tau}^2}. \tag{9}$$

Integrate (8) with respect to y^+ from the lower wall of the channel. The result is

$$\tau^+ + \frac{du^+}{dy^+} - \left(1 - \frac{y^+}{R_\tau}\right) = 0. \tag{10}$$

The turbulent shear stress is modeled using classical mixing length theory (von Karman;[11] see also Prandtl[12] and Driest[13]) Let

$$\tau^+ = \left(\lambda(y^+)\frac{du^+}{dy^+}\right)^2. \tag{11}$$

When (11) is substituted into (10), the result is a quadratic equation for du^+/dy^+. We use the positive root.

$$\frac{du^+}{dy^+} = -\frac{1}{2\lambda(y^+)^2} + \frac{1}{2\lambda(y^+)^2}\left(1 + 4\lambda(y^+)^2\left(1 - \frac{y^+}{R_\tau}\right)\right)^{1/2}. \tag{12}$$

Equation (12) is integrated from the wall to y^+ to obtain the velocity profile in the form of an integral dependent on the non-dimensional mixing length function $\lambda(y^+)$ at a given R_τ.

$$u^+(y^+) = \int_0^{y^+}\left(-\frac{1}{2\lambda(s)^2} + \frac{1}{2\lambda(s)^2}\left(1 + 4\lambda(s)^2\left(1 - \frac{s}{R_\tau}\right)\right)^{1/2}\right)ds. \tag{13}$$

At a low Reynolds number, (13) approaches the laminar pipe/channel flow solution

$$\lim_{R_\tau \to 0} u^+ = y^+\left(1 - \frac{y^+}{2R_\tau}\right), \tag{14}$$

where, in the laminar limit, $R_\tau = (2u_e\delta/\nu)^{1/2}$ where δ is the pipe radius or channel half height. The mixing length model introduced by Cantwell[1] to approximate pipe data is

$$\lambda(y^+) = \frac{ky^+\left(1 - e^{-\left(\frac{y^+}{a}\right)^m}\right)}{\left(1 + \left(\frac{y^+}{bR_\tau}\right)^n\right)^{1/n}}. \tag{15}$$

This model contains five free parameters. The constant k is closely related to the Kármán constant. The parameter a constitutes a wall damping length scale. The wall model is similar to the exponential decay proposed by van Driest[13] except for the exponent m that determines the rate of damping. The outer flow model includes a length scale b proportional to the fraction of the wall layer thickness where wake-like behavior begins, as well as an exponent n that helps shape the outer part of the profile. Near the wall

$$\lim_{y^+ \to 0} \lambda = ky^+\left(1 - e^{-\left(\frac{y^+}{a}\right)^m}\right). \tag{16}$$

The relatively small optimal value of $b = 0.1771$ and relatively large optimal value of $n = 2.4331$ for the boundary layer shown in Table I lead to the following approximate limiting behavior of the mixing length as the free stream is approached:

$$\lim_{y^+ \to R_\tau} \lambda \approx bkR_\tau. \tag{17}$$

This formulation of the velocity profile has several useful features.

- The velocity profile (13) with the mixing length model (15) is uniformly valid over $0 \le y \le \delta$ and $0 \le R_\tau < \infty$. So, there is no need for a buffer layer function, and there is no discontinuity in the velocity derivative at the outer edge of the boundary layer. At a low Reynolds number, the velocity profile reverts to the laminar solution.
- There is no presumption of logarithmic dependence of the velocity profile outside the viscous wall layer and so the profile can accurately approximate low Reynolds number wall layers.
- The profile is directly connected to a model of the turbulent shear stress that can be used in computations based on the full Reynolds Averaged Navier Stokes equations.
- Choosing optimal values of the model parameters (k, a, m, b, n) at a given R_τ enables subtle Reynolds number effects to be detected and compared. For example, in Table I there is a considerable variation in the parameter b between flow geometries indicating that the wake region in the boundary layer begins much closer to the wall than in channel or pipe flow. Distinct variations in the parameters k and a occur in pipe flow at low values of R_τ indicating an underlying change in turbulent structure. Similar variations do not seem to occur in the boundary layer although the data are limited.
- Nevertheless for a given flow geometry, the Reynolds number dependence of the model parameters (k, a, m, b, n) tends to be quite weak, and so average values of the model parameters can provide a good approximation to the velocity profile over a wide range of Reynolds numbers. This is true in pipe flow in spite of

TABLE I. Average model parameters for basic wall flows.

Flow	$\bar{k}$	$\bar{a}$	$\bar{m}$	$\bar{b}$	$\bar{n}$
Channel	0.4086	22.8673	1.2569	0.4649	1.3972
Pipe	0.4092	20.0950	1.6210	0.3195	1.6190
ZPG boundary layer	0.4194	24.8462	1.2043	0.1771	2.4331

the variations just described. This can be seen by examining Figs. 7, 13, and 14 in Cantwell.[1]

- Reynolds number scaling of various parts of the velocity, shear stress, and turbulent kinetic energy (TKE) production profiles is easily determined.
- The universal velocity profile defines an unambiguous overall thickness for the boundary layer. This will be called the *equivalent channel half height,* δ_h of the boundary layer. Throughout this paper, R_τ is defined as

$$R_\tau \equiv \frac{u_\tau \delta_h}{\nu}. \tag{18}$$

The equivalent channel half height concept will be described in detail in Sec. V.

- The universal velocity profile defines a threshold Reynolds number, $R_\tau > \approx 2000/k \approx 5000$, that distinguishes between high and low Reynolds number wall flow. State-of-the-art DNS computations can reach this range.
- With appropriate modeling, the universal profile can be applied to the wide range of turbulent diffusion problems involving the transport of temperature or a passive scalar where the transport equations are uncoupled from the velocity field.
- The accuracy of the fit to the velocity profile is such that extrapolation to Reynolds numbers beyond the range of available data can be used to explore the structure of the velocity profile in the limit of infinite Reynolds number.[1,14,15] This is the main topic of the present paper.

A final point: One of the most important problems in Large Eddy Simulation of wall flows has to do with the conflict between the need to reduce grid resolution near the wall in order to reduce computational cost and the requirement to accurately determine the wall friction at a given free stream velocity and wall position. The LES grid inevitably under-resolves the fine scale motions near the wall described in Sec. II that are responsible for generating the viscous layer and the wall shear stress. Efforts to resolve the viscous wall layer using empirical wall functions inevitably encounter the "log-layer mismatch" problem.[16,17] The universal profile provides an accurate value of the mean stream-wise and wall-normal velocity components, as well as the velocity derivative, wall friction, and turbulent shear stress throughout the viscous wall layer without assuming a log or power law profile and may provide a useful alternative to the current approach. Importantly, according to Subrahmanyam *et al.*,[3] the wall parameters (k, a, m) do not change in the presence of an adverse pressure gradient.

B. Optimal parameters

The accuracy of the universal velocity profile for pipe flow was demonstrated by Cantwell.[1] Similar accuracy for channel flow is demonstrated by Subrahmanyam *et al.*[2] In the case of a boundary layer on a flat plate, the flow variation in the stream-wise direction does not vanish and the boundary layer Eq. (6) does not simplify to one that is easily integrable. Although the universal velocity profile is not a solution of this equation Subrahmanyam *et al.*[2,3] show that the profile accurately fits DNS and experimental data for zero pressure gradient boundary layers as well as the adverse pressure gradient data of Perry and Marusic.[18]

The model parameters (k, a, m, b, n) for the mixing length function (15) are selected by minimizing the sum of total squared error between a given data profile and the universal velocity profile, (13), using the cost function

$$G = \sum_{i=1}^{N} (u^+(k, a, m, b, n, R_\tau, y_i^+) - u_i^+(y_i^+))^2. \tag{19}$$

Parameter values, $(\bar{k}, \bar{a}, \bar{m}, \bar{b}, \bar{n})$, averaged over a wide range of Reynolds numbers, for a smooth wall channel, pipe, and zero-pressure-gradient boundary layer flow are shown in Table I from Subrahmanyam *et al.*[2] Throughout this paper, the model constants are assumed to be the boundary layer average values shown in Table I, $(\bar{k}, \bar{a}, \bar{m}, \bar{b}, \bar{n}) = (0.4194, 24.8462, 1.2043, 0.1771, 2.4331)$. Although the universal profile was used to fit experimental data, the reason for using averages of only the DNS data here is that these profiles generally extend all the way to the wall and have lower uncertainty compared to experiments that generally do not resolve the lower part of the viscous wall layer. The boundary layer thickness reported by the various investigators who generated the DNS data were $\delta_{0.99}$, and this was used by Subrahmanyam *et al.*[2] to define δ_h and generate Table I. In Sec. V, it will be shown that a slightly larger value, 0.994, would actually produce slightly lower error in the fit of the universal velocity profile to the DNS data.

It should be noted that various constants given in this paper, such as those in Table I, are provided with a large number of significant figures so an interested reader can, if so desired, accurately reproduce the results presented here.

Figure 2 shows how the shape of the universal velocity profile becomes fuller as R_τ is increased by seven orders of magnitude. At the lowest Reynolds numbers, the profile is essentially the laminar channel/pipe velocity profile. At the highest Reynolds number, large increases produce very small changes in the velocity profile. At extreme Reynolds numbers, the velocity profile approaches plug flow, but astronomically large values are needed to approach this state.[1] Figure 3 shows the shape of the wall-normal velocity component nondimensionalized by the friction velocity. The fraction v/u_τ decreases by a factor of about 5 as R_τ is increased by five orders of magnitude.

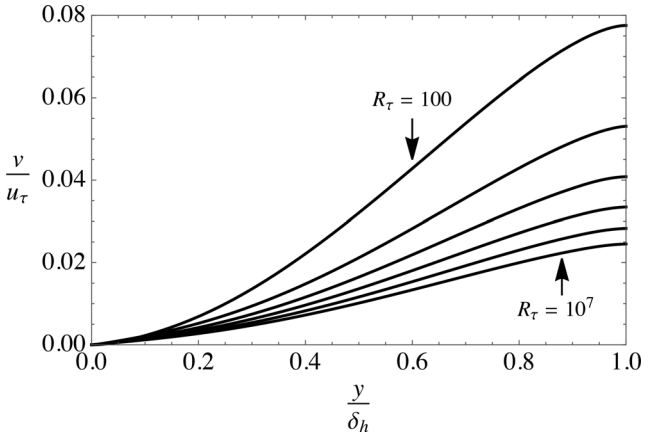

FIG. 3. The universal velocity profile, wall-normal velocity component at $R_\tau = 100, 1000, 10^4, 10^5, 10^6$, and 10^7.

Generally speaking, the parameters (k, a, m, b, n) depend weakly on the Reynolds number for a given flow geometry, and at a high Reynolds number, the dependence appears to be especially weak. The best evidence for this is the Princeton Superpipe data[19] that span three orders of magnitude in the Reynolds number.

Data for the boundary layer cover a much more limited range in comparison. Existing boundary layer evidence indicates that the parameters (k, a, m, b, n) depend at most weakly on the Reynolds number. However, the data are still quite limited, and flat plate data at a much higher Reynolds number are very much needed.

III. HIGH REYNOLDS NUMBER: THE TURBULENT BOUNDARY LAYER SHAPE FUNCTION

Equations (13) and (15) are repeated here with the full dependence on (k, a, m, b, n, R_τ) shown.

$$u^+(k, a, m, b, n, R_\tau, y^+) = \int_0^{y^+} \left(-\frac{1}{2\lambda^2} + \frac{1}{2\lambda^2}\left(1 + 4\lambda^2\left(1 - \frac{s}{R_\tau}\right)\right)^{1/2}\right) ds, \tag{20}$$

where

$$\lambda(k, a, m, b, n, R_\tau, y^+) = \frac{ky^+\left(1 - e^{-\left(\frac{y^+}{a}\right)^m}\right)}{\left(1 + \left(\frac{y^+}{bR_\tau}\right)^n\right)^{\frac{1}{n}}}. \tag{21}$$

Equations (20) and (21) admit a highly useful scaling that can be used to reduce the number of independent model parameters by one and determine the high Reynolds number limiting behavior of the boundary layer.[1,20] Use the group, $u/u_0 \to ku/u_0$, $y^+ \to ky^+$, and $R_\tau \to kR_\tau$ to define a modified wall-wake mixing length function by multiplying and dividing various terms in (21) by k.

$$\begin{aligned}\lambda(k, a, m, b, n, R_\tau, y^+) &= \frac{ky^+\left(1 - e^{-\left(\frac{y^+}{a}\right)^m}\right)}{\left(1 + \left(\frac{y^+}{bR_\tau}\right)^n\right)^{\frac{1}{n}}} \\ &= \frac{ky^+\left(1 - e^{-\left(\frac{ky^+}{ka}\right)^m}\right)}{\left(1 + \left(\frac{ky^+}{b(kR_\tau)}\right)^n\right)^{\frac{1}{n}}} \\ &= \tilde{\lambda}(ka, m, b, n, kR_\tau, ky^+).\end{aligned} \tag{22}$$

In the reduced space, k and a are not independent parameters. Multiply both sides of (20) by k and insert the modified mixing length function (22). Choose the integration variable, $\alpha = ky^+$.

$$ku^+ = \int_0^{ky^+} \left(-\frac{1}{2\tilde{\lambda}^2} + \frac{1}{2\tilde{\lambda}^2}\left(1 + 4\tilde{\lambda}^2\left(1 - \frac{\alpha}{kR_\tau}\right)\right)^{1/2}\right) d\alpha. \tag{23}$$

Equation (23) can be viewed as a k independent model velocity profile, ku^+, with four model parameters, (ka, m, b, n) in a boundary layer at the scaled friction Reynolds number, kR_τ. Now, define the boundary layer shape function.

$$\Phi(ka, b, m, n, kR_\tau, ky^+) = \int_0^{ky^+} \left(-\frac{1}{2\tilde{\lambda}^2} + \frac{1}{2\tilde{\lambda}^2}\left(1 + 4\tilde{\lambda}^2\left(1 - \frac{\alpha}{kR_\tau}\right)\right)^{1/2}\right) d\alpha - ln(ky^+). \tag{24}$$

Note that $ky^+ = (y/\delta_h)kR_\tau$ where δ_h is the boundary layer overall thickness, to be defined precisely a little later. The shape function, (24), has the remarkable property that, for fixed (y/δ_h), it approaches a constant value as $kR_\tau \to \infty$.

$$\lim_{kR_\tau \to \infty} \Phi(ka, b, m, n, kR_\tau, (y/\delta_h)kR_\tau)|_{y/\delta_h = const} = \phi(ka, b, m, n, y/\delta_h). \tag{25}$$

Importantly, the limit is approached quite rapidly, and for $kR_\tau > 2000$, the limit is fully established over almost the entire thickness of the boundary layer except very close to the wall. Figure 4 illustrates this behavior. The limiting shape function, ϕ, is shown in Fig. 5. Figure 5 is essentially a cut through Fig. 4 at some value kR_τ considerably larger than 2000. We will use (25) in two ways: first to develop an easy-to-use expression for the outer flow velocity profile at a high Reynolds number and second, to determine the high Reynolds number behavior of the integral properties of the flow. The condition $R_\tau > 2000/k \approx 5000$ is an inherent property of the universal velocity profile and can be understood as defining a threshold between high and low Reynolds number wall flow.

IV. THE FRICTION LAW AND BOUNDARY LAYER INTEGRAL MEASURES AT A HIGH REYNOLDS NUMBER

According to (23)–(25), at Reynolds numbers larger than $kR_\tau \cong 2000$ or so, the velocity profile can be accurately approximated by

$$\lim_{kR_\tau > 2000} u^+ = \frac{1}{k}\ln(ky^+) + \frac{1}{k}\phi\left(ka, m, b, n, \frac{y}{\delta_h}\right). \tag{26}$$

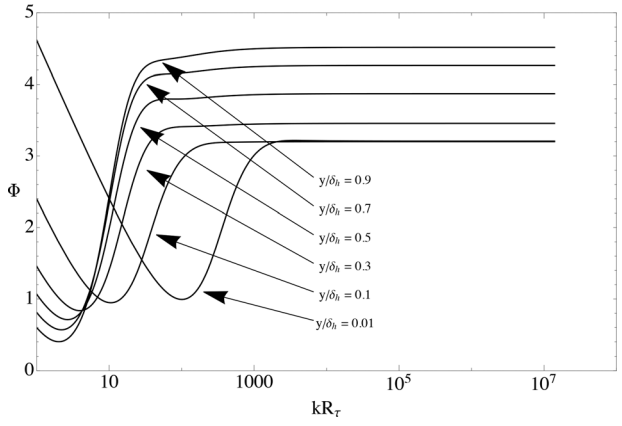

FIG. 4. Boundary layer shape function, Eq. (24), at various values of y/δ_h. For $kR_\tau > 2000$ the shape function is independent of R_τ except very close to the wall.

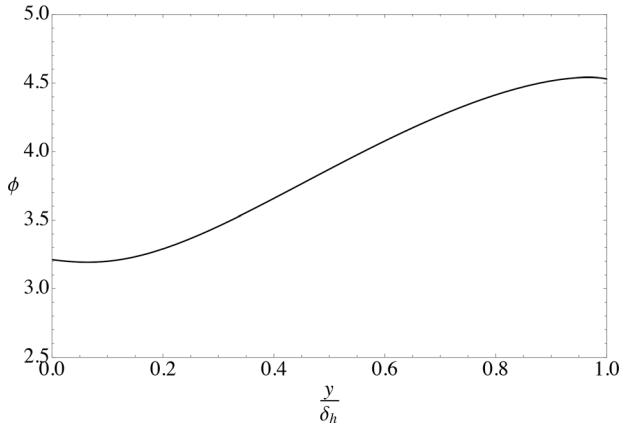

FIG. 5. High Reynolds number limit of the boundary layer shape function, Eq. (25).

Evaluating (26) at the boundary layer edge generates the high Reynolds number friction law.

$$\frac{u_e}{u_\tau} = \frac{1}{k}\ln(kR_\tau) + \frac{1}{k}\phi(ka, m, b, n, 1),$$
$$\frac{u_e}{u_\tau} = 2.384359\ln(R_\tau) + 8.731260. \tag{27}$$

Divide (26) by (27) and let $ky^+ = (y/\delta_h)kR_\tau$. The result is

$$\lim_{kR_\tau>2000}\frac{u}{u_e} = \frac{\phi(ka, m, b, n, y/\delta_h) + \ln(y/\delta_h) + \ln(kR_\tau)}{\phi(ka, m, b, n, 1) + \ln(kR_\tau)}. \tag{28}$$

The high Reynolds number form of the velocity profile (28) can be used to generate the high Reynolds number behavior of all the integral measures of the boundary layer as functions of R_τ. Let $\eta = y/\delta_h$. The needed relevant constants generated by $\phi(ka, m, b, n, \eta)$ are as follows.

$$C_1 \equiv \phi(ka, m, b, n, 1) = 4.530802,$$
$$C_2 \equiv \int_0^1 \phi(ka, m, b, n, \eta)d\eta = 3.861861,$$
$$C_3 \equiv \int_0^1 \phi(ka, m, b, n, \eta)^2 d\eta = 15.149878,$$
$$C_4 \equiv \int_0^1 \phi(ka, m, b, n, \eta)^3 d\eta = 60.327378,$$
$$C_5 \equiv \int_0^1 \ln(\eta)\phi(ka, m, b, n, \eta)d\eta = -3.459397, \tag{29}$$
$$C_6 \equiv \int_0^1 \ln(\eta)\phi(ka, m, b, n, \eta)^2 d\eta = -12.092035,$$
$$C_7 \equiv \int_0^1 \ln(\eta)^2\phi(ka, m, b, n, \eta)d\eta = 6.578894,$$
$$C_8 \equiv \int_0^1 \ln(\eta)^2\phi(ka, m, b, n, \eta)^2 d\eta = 21.719529.$$

As noted earlier, the constants listed in Eq. (29) and elsewhere in this paper are presented with a large number of significant figures, so an interested reader can accurately reproduce the results presented. The constants generated by the boundary layer shape function will be used to determine the high Reynolds number behavior of the integral measures of the boundary layer as functions of R_τ. We also need integrals of powers of the logarithm, $\int_0^1 \ln(\eta)d\eta = -1$, $\int_0^1 \ln(\eta)^2 d\eta = 2$, $\int_0^1 \ln(\eta)^3 d\eta = -6$. Integrals of the first three powers of the velocity profile can now be generated.

$$\lim_{kR_\tau>2000}\int_0^1\left(\frac{u}{u_e}\right)d\eta$$
$$= \frac{u_\tau}{ku_e}\int_0^1\left(\phi(ka, m, b, n, \eta) + \ln(\eta) + \ln(kR_\tau)\right)d\eta$$
$$= \frac{u_\tau}{ku_e}(\ln(kR_\tau) + C_2 - 1) = \frac{\ln(kR_\tau) + C_2 - 1}{\ln(kR_\tau) + C_1}. \tag{30}$$

$$\lim_{kR_\tau>2000}\int_0^1\left(\frac{u}{u_e}\right)^2 d\eta$$
$$= \left(\frac{u_\tau}{ku_e}\right)^2\int_0^1\Big[\phi(ka, m, b, n, \eta)^2 + \ln(\eta)^2 + \ln(kR_\tau)^2$$
$$+ 2\ln(kR_\tau)\phi(ka, m, b, n, \eta) + 2\ln(kR_\tau)\ln(\eta)$$
$$+ 2\ln(\eta)\phi(ka, m, b, n, \eta)\Big]d\eta$$
$$= \left(\frac{u_\tau}{ku_e}\right)^2(\ln(kR_\tau)^2 + 2(C_2 - 1)\ln(kR_\tau) + 2 + C_3 + 2C_5)$$
$$= \frac{\ln(kR_\tau)^2 + 2(C_2 - 1)\ln(kR_\tau) + 2 + C_3 + 2C_5}{(\ln(kR_\tau) + C_1)^2}. \tag{31}$$

$$\lim_{kR_\tau>2000}\int_0^1\left(\frac{u}{u_e}\right)^3 d\eta$$
$$= \left(\frac{u_\tau}{ku_e}\right)^3\int_0^1\big[\ln(kR_\tau)^3 + 3\ln(kR_\tau)^2\phi + 3\ln(kR_\tau)\phi^2$$
$$+ \phi^3 + 3\ln(kR_\tau)^2\ln(\eta) + 6\ln(kR_\tau)\ln(\eta)\phi + 3\ln(\eta)\phi^2$$
$$+ 3\ln(kR_\tau)\ln(\eta)^2 + 3\ln(\eta)^2\phi + \ln(\eta)^3\big]d\eta$$
$$= \left(\frac{u_\tau}{ku_e}\right)^3(\ln(kR_\tau)^3 + 3C_2\ln(kR_\tau)^2 + 3C_3\ln(kR_\tau)$$
$$+ C_4 - 3\ln(kR_\tau)^2 + 6C_5\ln(kR_\tau) + 3C_6$$
$$+ 6\ln(kR_\tau) + 3C_7 - 6)$$
$$= \frac{\ln(kR_\tau)^3 + 3(C_2 - 1)\ln(kR_\tau)^2 + 3(C_3 + 2C_5 + 2)\ln(kR_\tau)}{(\ln(kR_\tau) + C_1)^3}$$
$$+ \frac{C_4 + 3C_6 + 3C_7 - 6}{(\ln(kR_\tau) + C_1)^3}. \tag{32}$$

This process could be continued to include the integral of any power of (u/u_e) generating additional powers of $\ln(R_\tau)$ in the process.

Use Eq. (30) to form the displacement thickness.

$$\lim_{kR_\tau>2000}\frac{\delta_1}{\delta_h}=\lim_{kR_\tau>2000}\int_0^1\left(1-\frac{u}{u_e}\right)d\eta=\frac{1+C_1-C_2}{\ln(kR_\tau)+C_1}$$
$$=\frac{1.668940}{\ln(kR_\tau)+4.530802}. \tag{33}$$

Use Eqs. (30) and (31) to form the momentum thickness.

$$\lim_{kR_\tau>2000}\frac{\delta_2}{\delta_h}=\lim_{kR_\tau>2000}\int_0^1\frac{u}{u_e}\left(1-\frac{u}{u_e}\right)d\eta$$
$$=\frac{(1+C_1-C_2)\ln(kR_\tau)-2-C_1-C_3-2C_5+C_1C_2}{(\ln(kR_\tau)+C_1)^2}$$
$$=\frac{1.668940\ln(kR_\tau)+2.735444}{(\ln(kR_\tau)+4.530802)^2}. \tag{34}$$

Use Eqs. (30) and (32) to form the energy thickness.

$$\lim_{kR_\tau>2000}\frac{\delta_3}{\delta_h}=\lim_{kR_\tau>2000}\int_0^1\frac{u}{u_e}\left(1-\left(\frac{u}{u_e}\right)^2\right)d\eta$$
$$=\frac{2(1+C_1-C_2)\ln(kR_\tau)^2}{(\ln(kR_\tau)+C_1)^3}$$
$$+\frac{(-6-2C_1+{C_1}^2+2C_1C_2-3C_3-6C_5)\ln(kR_\tau)}{(\ln(kR_\tau)+C_1)^3}$$
$$+\frac{6-{C_1}^2+{C_1}^2C_2-C_4-3C_6-3C_7}{(\ln(kR_\tau)+C_1)^3}$$
$$=\frac{2(1.668940)\ln(kR_\tau)^2+3.767969\ln(kR_\tau)+20.960809}{(\ln(kR_\tau)+4.530802)^3}. \tag{35}$$

Note that δ_1/δ_h, δ_2/δ_h and δ_3/δ_h all vary as $1/\ln(kR_\tau)$ as $R_\tau\to\infty$, suggesting an extremely slow decrease at a high Reynolds number. This accounts for the very slow changes in the velocity profile at a high Reynolds number seen in Fig. 2.

The thickness ratios (33) and (34) can be used to generate the high Reynolds number behavior of the momentum shape factor, δ_1/δ_2,

$$\lim_{kR_\tau>2000}\frac{\delta_1}{\delta_2}=\frac{(1+C_1-C_2)(\ln(kR_\tau)+C_1)}{(1+C_1-C_2)\ln(kR_\tau)-2-C_1-C_3-2C_5+C_1C_2}$$
$$=\frac{1.668940(\ln(kR_\tau)+4.530802)}{1.668940\ln(kR_\tau)+2.735444} \tag{36}$$

with an infinite Reynolds number limit of 1. Use (35) to generate the inverse of the energy shape factor δ_1/δ_3 at a high Reynolds number.

$$\lim_{kR_\tau>2000}\frac{\delta_3}{\delta_1}=\frac{2(1+C_1-C_2)\ln(kR_\tau)^2}{(1+C_1-C_2)(\ln(kR_\tau)+C_1)^2}$$
$$+\frac{(-18-2C_1+{C_1}^2+2C_1C_2-3C_3-6C_5)\ln(kR_\tau)}{(1+C_1-C_2)(\ln(kR_\tau)+C_1)^2}$$
$$+\frac{6-{C_1}^2+{C_1}^2C_2-C_4-3C_6-3C_7}{(1+C_1-C_2)(\ln(kR_\tau)+C_1)^2}$$
$$=\frac{2(1.668940)\ln(kR_\tau)^2+3.767969\ln(kR_\tau)+20.960809}{1.668940(\ln(kR_\tau)+4.530802)^2}, \tag{37}$$

with an infinite Reynolds number limit of 2. The inverse Eq. (37) is presented simply because it can be written as three separate terms over a common denominator to fit the column format.

A. The friction law and thickness Reynolds numbers vs R_τ in the range $0 \le R_\tau \le 10^7$

The friction law and thickness Reynolds numbers generated by the universal velocity profile over the entire range of Reynolds numbers are shown as solid lines in Figs. 6–15. These results will be used in Sec. VII to integrate the Karman Eq. (1) in order to generate the integral boundary layer properties in x. The dotted lines in these figures are the Blasius solution for comparison with the low Reynolds number and transitional behavior of the boundary layer. The dashed lines are the high Reynolds number behavior of each of the quantities displayed. Note that in all cases, high Reynolds number behavior is clearly reached for $R_\tau >\approx 5000$.

1. The friction law

The boundary layer friction law,

$$\frac{u_e}{u_\tau}=\int_0^{R_\tau}\left(-\frac{1}{2\lambda(s)^2}+\frac{1}{2\lambda(s)^2}\left(1+4\lambda(s)^2\left(1-\frac{s}{R_\tau}\right)\right)^{1/2}\right)ds\equiv F_1(R_\tau), \tag{38}$$

is shown in Fig. 6. The high Reynolds number limit given in Eq. (27) is indicated by the dashed line in Fig. 6.

2. Displacement thickness Reynolds number

The displacement thickness Reynolds number expressed in wall units

$$R_{\delta_1}=\frac{u_e\delta_1}{\nu}=\frac{u_e}{u_\tau}\int_0^{R_\tau}\left(1-\frac{u_\tau}{u_e}u^+\right)dy^+\equiv F_2(R_\tau), \tag{39}$$

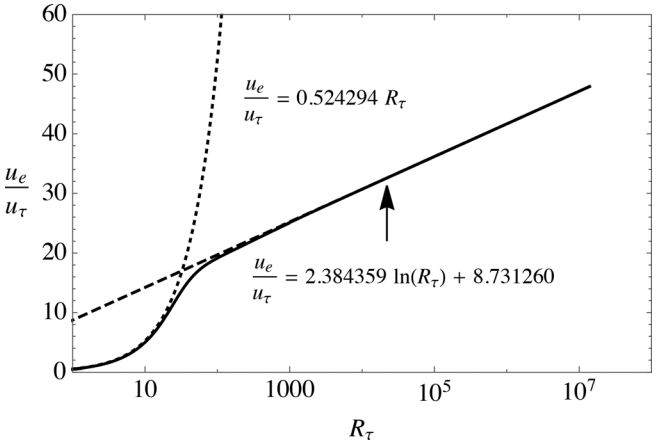

FIG. 6. Friction law generated by the universal velocity profile, $F_1(R_\tau)$. The dotted line is the Blasius solution. The dashed line is the high Reynolds number limit given in Eq. (27).

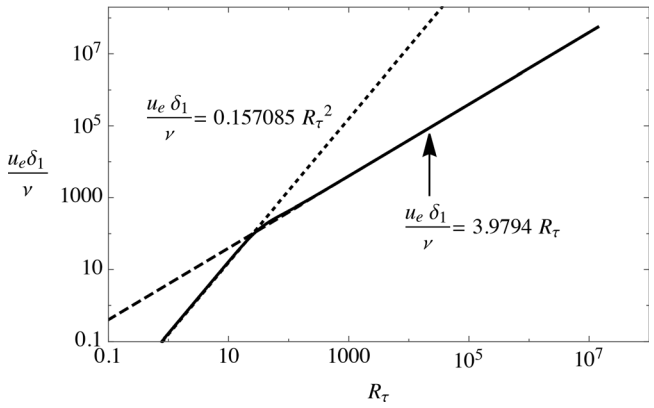

FIG. 7. Displacement thickness Reynolds number, $F_2(R_\tau)$ generated using the universal velocity profile. The dotted line is the Blasius profile. The dashed line is the high Reynolds number limit given in Eq. (40).

is shown as the solid line in Fig. 7. The high Reynolds number, $kR_\tau > 2000$, limit of (39) is generated from (27) and (33) as follows:

$$\lim_{kR_\tau>2000} R_{\delta_1} \equiv \frac{u_e\delta_1}{\nu} = \frac{ku_e}{u_\tau}\frac{\delta_1}{\delta_h}\frac{R_\tau}{k} = \frac{1+C_1-C_2}{k}R_\tau = 3.9794R_\tau. \tag{40}$$

Equation (40) is plotted as the dashed line in Fig. 7 and shows the highly interesting result that at a high Reynolds number, R_{δ_1} is linearly proportional to R_τ with no logarithmic factor present. Using (40), we can write

$$\lim_{kR_\tau>2000}\frac{\delta_h}{\delta_1} = \frac{k}{1-C_1-C_2}\frac{u_e}{u_\tau} = \frac{1}{3.9794}\frac{u_e}{u_\tau}, \tag{41}$$

providing a direct connection between the friction velocity and δ_1 at a high Reynolds number.

3. Momentum thickness Reynolds number

The momentum thickness Reynolds number can also be written in terms of wall units as

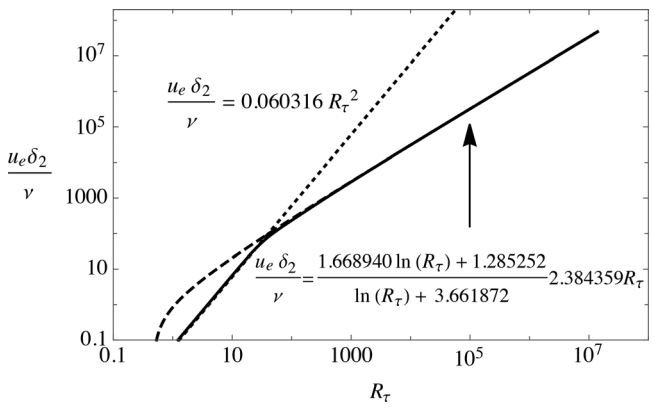

FIG. 8. Momentum thickness Reynolds number, $F_3(R_\tau)$ generated using the universal velocity profile. The dotted line is the Blasius profile. The dashed line is the high Reynolds number limit given in Eq. (43).

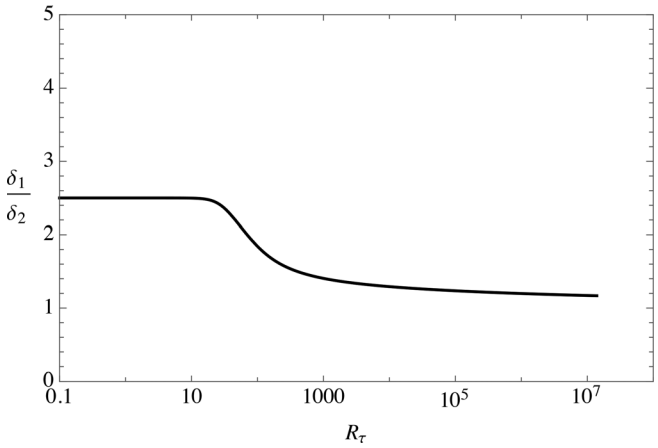

FIG. 9. Momentum shape factor generated by the universal velocity profile. At low Reynolds number, the shape factor approaches the channel flow value, $H_{channel} = 2.5$, which can be compared to the Blasius value of 2.604. The high Reynolds number limit is 1.0.

$$R_{\delta_2} = \frac{u_e\delta_2}{\nu} = \int_0^{R_\tau} u^+\left(1-\frac{u_\tau}{u_e}u^+\right)dy^+ \equiv F_3(R_\tau), \tag{42}$$

and is shown in Fig. 8.

The high Reynolds number momentum thickness is constructed as follows:

$$\begin{aligned}\lim_{kR_\tau>2000} R_{\delta_2} &\equiv \frac{u_e\delta_2}{\nu}\\ &= \frac{ku_e}{u_\tau}\frac{\delta_2}{\delta_h}\frac{R_\tau}{k}\\ &= \left(\frac{(1+C_1-C_2)\ln(kR_\tau)-2-C_1-C_3-2C_5+C_1C_2}{\ln(kR_\tau)+C_1}\right)\frac{R_\tau}{k}\\ &= \left(\frac{1.668940\ln(kR_\tau)+2.735444}{\ln(kR_\tau)+4.530802}\right)2.384359R_\tau.\end{aligned} \tag{43}$$

The momentum shape factor, $H_{12} = \delta_1/\delta_2$, is shown in Fig. 9. Note the very slow approach of H_{12} to one due to the logarithmic behavior in Eq. (43).

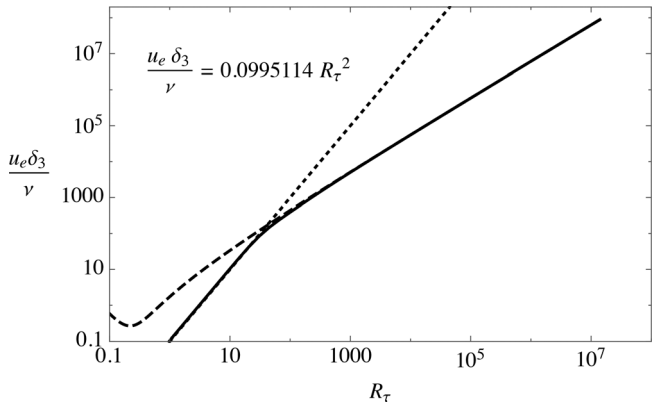

FIG. 10. Energy thickness Reynolds number generated using the universal velocity profile. The dotted line is the Blasius profile. The dashed line is the high Reynolds number behavior (45) determined from the shape function.

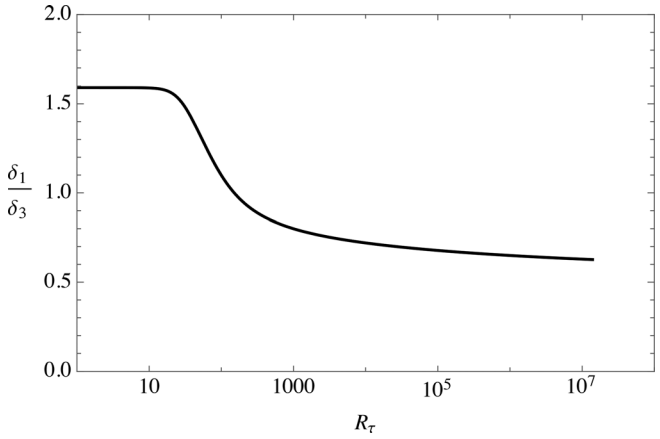

FIG. 11. The energy shape factor δ_1/δ_3. At a low Reynolds number, the shape factor approaches the channel flow value, $H_{13,channel} = 105/66$, which can be compared to the Blasius value of 1.579. The high Reynolds number limit is 1/2.

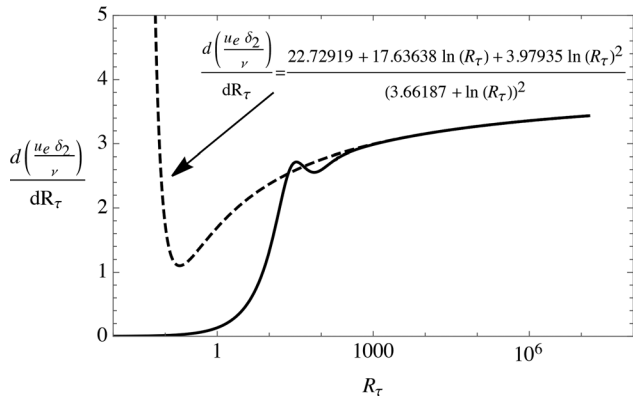

FIG. 12. Derivative of the momentum thickness Reynolds number, Eq. (48). The dashed line is the derivative of the high Reynolds number approximation Eq. (43).

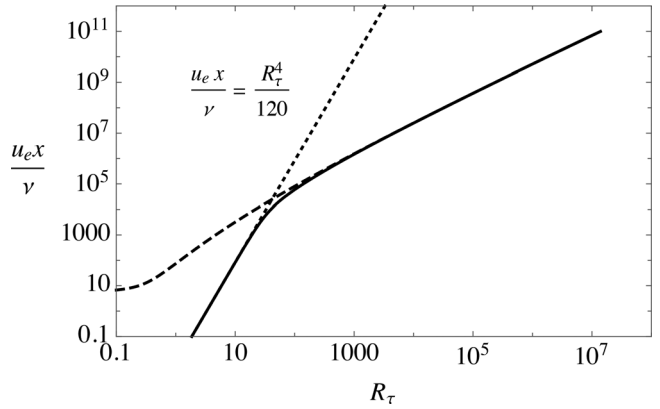

FIG. 13. Integral of Eq. (47) relating R_x to R_τ generated by integrating Eq. (47). The dotted line is the Blasius profile. The dashed line is the integral (53).

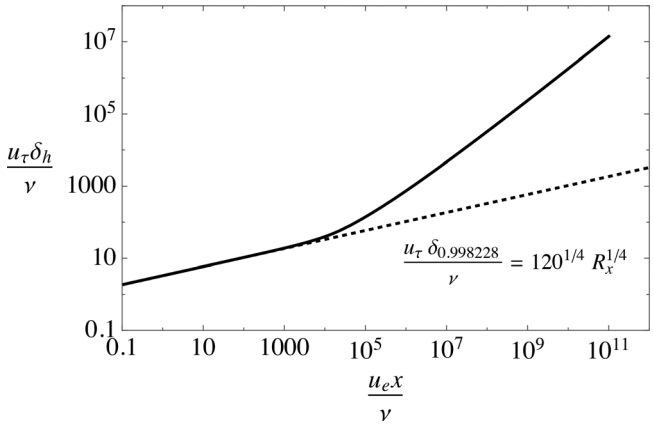

FIG. 14. Function F_6 relating R_τ to R_x generated by integrating and inverting Eq. (47). The dotted line is the Blasius profile.

4. Energy thickness Reynolds number

The energy thickness Reynolds number in terms of wall units is

$$R_{\delta_3} = \frac{u_e\delta_3}{\nu} = \int_0^{R_\tau} u^+\left(1 - \left(\frac{u_\tau}{u_e}\right)^2 u^{+2}\right)dy^+ \equiv F_4(R_\tau). \tag{44}$$

At a high Reynolds number

$$\begin{aligned}\lim_{kR_\tau>2000} R_{\delta_3} \equiv \frac{u_e\delta_3}{\nu} &= \frac{ku_e}{u_\tau}\frac{\delta_3}{\delta_h}\frac{R_\tau}{k} = \frac{2(1+C_1-C_2)\ln(kR_\tau)^2}{(\ln(kR_\tau)+C_1)^2}\frac{R_\tau}{k}\\ &+\frac{(-6-2C_1+{C_1}^2+2C_1C_2-3C_3-6C_5)\ln(kR_\tau)}{(\ln(kR_\tau)+C_1)^2}\frac{R_\tau}{k}\\ &+\frac{6-{C_1}^2+{C_1}^2C_2-C_4-3C_6-3C_7}{(\ln(kR_\tau)+C_1)^2}\frac{R_\tau}{k}\\ &=\frac{2(1.668940)\ln(kR_\tau)^2+3.767969\ln(kR_\tau)+20.960809}{(\ln(kR_\tau)+4.530802)^2}\\ &\times 2.384359R_\tau.\end{aligned} \tag{45}$$

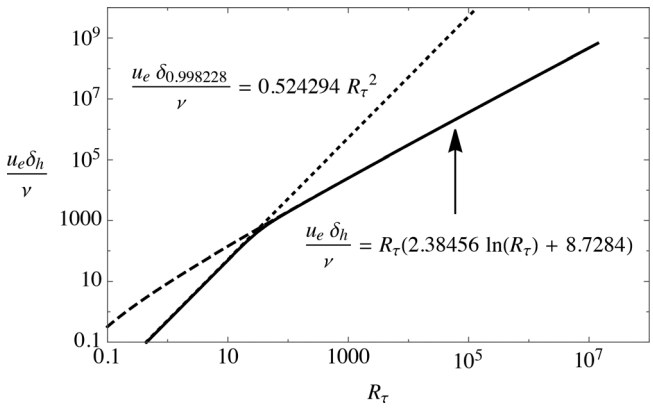

FIG. 15. Equivalent channel half height Reynolds number, Eq. (55), generated by the universal velocity profile. The Blasius thickness, $\delta_{0.998228}$, equates the friction Reynolds number of the channel flow and Blasius profiles. The dotted line is the Blasius profile. The dashed line is the friction law Eq. (27) multiplied by R_τ.

The energy shape factor, $H_{13} = \delta_1/\delta_3$, is shown in Fig. 11. Similar to the momentum shape factor, the very slow approach of H_{13} to the limit 1/2 is due to the logarithmic behavior in Eq. (45).

5. Relationship between R_τ and R_x

To determine how the boundary layer grows in space, we now integrate the zero pressure gradient form of the von Kaŕmań equation.[5]

$$\frac{d\delta_2}{dx} = \frac{C_f}{2} = \left(\frac{u_\tau}{u_e}\right)^2. \tag{46}$$

Equation (46) can be rearranged to read

$$dR_x = \frac{dR_{\delta_2}}{dR_\tau}\left(\frac{u_e}{u_\tau}\right)^2 dR_\tau = \left({F_1}^2 F_5\right) dR_\tau. \tag{47}$$

The derivative,

$$\frac{dR_{\delta_2}}{dR_\tau} \equiv F_5(R_\tau), \tag{48}$$

is shown in Fig. 12. The high Reynolds number limit of Eq. (48) is

$$\lim_{kR_\tau > 2000} \frac{dR_{\delta_2}}{dR_\tau} = \frac{22.72919 + 17.63638\ln(R_\tau) + 3.97935\ln(R_\tau)^2}{(3.66187 + \ln(R_\tau))^2}, \tag{49}$$

shown as the dashed line in Fig. 12. Note how rapidly the full integration of the universal profile (solid line) approaches the high Reynolds number limit (dashed line) in this figure.

The integral of (47) is shown as the solid line in Fig. 13. The high Reynolds number limit of the integral can be determined by combining (27), (43), (47), and (48). The high Reynolds number form of Eq. (47) is

$$\lim_{kR_\tau > 2000} \frac{dR_x}{dR_\tau} = \alpha + \beta\ln(R_\tau) + \gamma ln(R_\tau)^2, \tag{50}$$

where

$$\begin{aligned}\alpha &= \frac{1}{k^3}(2 - 2C_1C_2 + C_1^2C_2 + C_3 - C_1C_3 + 2C_5 \\ &\quad -2C_1C_5 - (2 - {C_1}^2 + C_3 + 2C_5)\ln(k) \\ &\quad + (1 + C_1 - C_2)\ln(k)^2) \\ \beta &= \frac{1}{k^3}(-2 + C_1^2 - C_3 - 2C_5 + 2(1 + C_1 - C_2)\ln(k)) \\ \gamma &= \frac{1}{k^3}(1 + C_1 - C_2).\end{aligned} \tag{51}$$

The integral of (50) is

$$\lim_{kR_\tau > 2000} R_x = (\alpha - \beta + 2\gamma + (\beta - 2\gamma)\ln(R_\tau) + \gamma ln(R_\tau)^2)R_\tau. \tag{52}$$

Evaluating the constants, the result is

$$\lim_{kR_\tau > 2000} R_x = (3.2798 + 2.4320\ln(R_\tau) + \ln(R_\tau)^2)22.6233R_\tau, \tag{53}$$

shown as a dashed curve in 13. The integral of (47) also generates the inverse relation between R_τ and R_x shown in Fig. 14, which we will need in Sec. VII.

$$R_\tau = F_6(R_x). \tag{54}$$

The functions F_1, F_2, F_3, and F_4 define the integral properties of the flow while F_5 and F_6 provide the required equations needed to characterize the spatial evolution of the boundary layer along the wall. What remains is simply to replace R_τ with $F_6(R_x)$ in F_1, F_2, F_3, and F_4. However, before doing so, it is necessary to precisely define the overall boundary layer thickness, δ_h.

V. THE BOUNDARY LAYER EQUIVALENT CHANNEL HALF HEIGHT

It is clear from the results so far that the friction Reynolds number, R_τ, is the natural choice for characterizing wall-bounded flows. However, R_τ is often avoided because the thickness of the boundary layer is not well defined. As noted earlier, it requires that the boundary layer is cut off at some point in the velocity profile where $u/u_e = 0.99$ or 0.999 or some other arbitrary choice leading to a considerable variation in the overall thickness, δ, used to characterize the layer. This does not need to be the case, and it will be shown in this section that when the universal velocity profile is used to approximate the velocity profile an outer length scale for the boundary layer is effectively defined.

Multiply both sides of Eq. (38) by R_τ, so it reads

$$\frac{u_e\delta_h}{\nu} = R_\tau F_1(R_\tau) \equiv F_7(R_\tau). \tag{55}$$

The function F_7 is plotted as the solid line in Fig. 15. The δ_h that appears in (55) is the channel half height of the profile and $u_e\delta_h/\nu$ will be called the equivalent channel half height Reynolds number of the boundary layer, R_{δ_h}. Figure 15 shows how this Reynolds number depends on R_τ.

The main takeway from Figs. 6–15 is that all of the integral measures of the turbulent boundary layer at a high Reynolds number except the displacement thickness are directly proportional to a factor involving $\ln(kR_\tau)$ multiplied by R_τ. In addition, all the asymptotic behaviors, Eqs. (27), (39), (43), and (45) are reached close to, or even slightly below, the threshold Reynolds number of $kR_\tau > 2000$, which is not all that high in the scheme of things and, as pointed out earlier, can be reached by DNS computations today.

A. The laminar pipe profile compared to Blasius

The basic idea behind δ_h is to choose the value that minimizes the error between the universal velocity profile and the data. The details of this discussion as regards the turbulent boundary layer will be filled in shortly, but first it is necessary to look at the laminar portion of the flow.

Notice that in Fig. 15, the channel flow half height Reynolds number is compared with the Blasius thickness Reynolds number corresponding to a very specific laminar thickness where $u/u_e = 0.998228$. The reasoning behind this is as follows.

In the boundary layer integral method presented here, the universal velocity profile will be used throughout, including in the laminar boundary layer near the origin of the flow. In Figs. 6, 7, 8, 10, and 13–15, the Blasius limit is provided for comparison. However, what Blasius profile is this? In particular, what boundary layer thickness is used to make the comparison, what is the corresponding skin friction

comparison, and how is the Blasius boundary layer Reynolds number related to the equivalent channel flow Reynolds number?

At small values of R_τ, the limiting behavior of F_1 and F_5 is the channel flow limit.

$$\lim_{R_\tau \to 0} F_1 = \frac{R_\tau}{2}, \tag{56}$$

and

$$\lim_{R_\tau \to 0} F_5 = \frac{2R_\tau}{15}. \tag{57}$$

In this limit, Eq. (47) becomes

$$dR_x = \frac{{R_\tau}^3}{30} dR_\tau. \tag{58}$$

Near the origin of the flow, at small values of R_τ and R_x, the universal velocity profile inserted in (47) leads to

$$\lim_{R_x \to 0} R_{\tau_{channel}} = \frac{u_\tau \delta_h}{\nu} = 120^{1/4} \left(\frac{u_e x}{\nu}\right)^{1/4} = 3.30975 \left(\frac{u_e x}{\nu}\right)^{1/4}. \tag{59}$$

The Blasius profile can also be expressed in terms of R_τ, and here is where $\delta_{0.998228}$ comes in. With this choice, the Blasius thickness Reynolds number is

$$\frac{u_e \delta_{0.998228}}{\nu} = 5.743355 \left(\frac{u_e x}{\nu}\right)^{1/2}. \tag{60}$$

The Blasius friction law, $C_f = 0.6641854/{R_x}^{1/2}$, can be expressed in terms of the friction velocity as

$$\frac{u_\tau}{u_e} = (0.3320927)^{1/2} \left(\frac{u_e x}{\nu}\right)^{-1/4}. \tag{61}$$

The Blasius friction Reynolds number is the product of (60) and (61) generating

$$\lim_{R_x \to 0} R_{\tau_{Blasius}} = \frac{u_\tau \delta_{0.998228}}{\nu} = 3.30975 \left(\frac{u_e x}{\nu}\right)^{1/4}, \tag{62}$$

which precisely matches Eq. (59). This approach matches the channel flow friction Reynolds number to the Blasius friction Reynolds number throughout the laminar part of the flow. However, it should be noted that at the same freestream velocity and streamwise position, the two flows do not have the same wall shear stress. To clarify this, Eqs. (55), (56), (59), and (61) can be combined to show that

$$\frac{\left(\frac{u_\tau}{u_e}\right)_{channel}}{\left(\frac{u_\tau}{u_e}\right)_{Blasius}} = \frac{2}{1.90733} = 1.04859. \tag{63}$$

Since

$$R_{\tau_{Blasius}} = R_{\tau_{channel}} \Rightarrow u_{\tau channel} \delta_h = u_{\tau Blasius} \delta_{0.998228}, \tag{64}$$

the thicknesses must also be in the ratio

$$\frac{\delta_{0.998228}}{\delta_h} = 1.04859. \tag{65}$$

The point in the $\delta_{0.998228}$ Blasius velocity profile corresponding to the point δ_h in the channel profile where $u_{channel}/u_e = 1$ is $u_{Blasius}/u_e = 0.996798$. The corresponding channel and Blasius profiles are shown in Fig. 16 with these details identified. The upshot of this is that using the universal velocity profile in the laminar region overestimates the wall shear stress by about 10%.

In his classic textbook on fluid mechanics, White[21] teaches a method used by von Kármán to generate approximate solutions for the integral properties of the laminar boundary layer. The method is essentially the same as the one used here where the approximations are all generated from the exact laminar quadratic channel/pipe flow velocity profile,

$$\frac{u}{u_e} = \frac{y}{\delta_h}\left(2 - \frac{y}{\delta_h}\right), \tag{66}$$

where u_e is the pipe or channel centerline velocity and δ_h is the channel half width or pipe radius. The main difference is that in White[21] and in other text books where von Kármán's simplification is presented, the Blasius boundary layer thickness used for the integration is the point where $u/u_e = 0.99$ rather than $u/u_e = 0.998228$ used here to ensure that both flows have the same R_τ.

This subject has been revisited recently by Majdalani and Xuan,[22] who develop improved higher order polynomial approximations to the Blasius profile for application to integral analyses of laminar viscous and thermal problems. They provide a detailed comparison between several methods for approximating the Blasius solution.

It should be noted here that the "Blasius constant," $\sigma = 0.46959999$,[22] which is essentially the normalized wall shear stress can be determined to arbitrary accuracy by using the invariance of the Blasius ODE under a one parameter dilation group. The procedure is described in detail on page 292 of Cantwell.[20] The idea is to carry out one high precision computation of the Blasius equation as a Cauchy initial value problem with an arbitrary initial choice of σ, say $\sigma = 0.2$. The computed (too small) free stream velocity is used to evaluate the group parameter needed to scale the numerical solution to the exact free stream boundary condition $u/u_e = 1$. A refined value of the Blasius constant generated using the group approach is $\sigma = 0.46959998836101335406567 61$. To

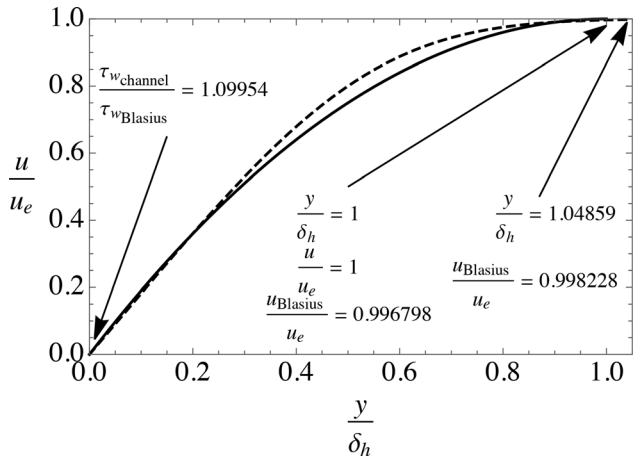

FIG. 16. Blasius velocity profile compared to channel flow at the same value of R_τ. The dashed line is the Blasius profile.

determine this value, the Blasius equation is integrated out to $5\alpha_{0.99}$ where $\alpha = y(U/2\nu x)^{1/2}$ is the Blasius similarity variable.

B. The equivalent channel half height for the turbulent boundary layer

The fact that the universal velocity profile accurately fits a given turbulent boundary layer data set enables the boundary layer equivalent channel half height, δ_h, to be determined. The equivalent channel half height defines a point where $u/u_e = 1$ and $\partial u/\partial y = 0$ at $y/\delta_h = 1$. Since the universal profile is fundamentally a pipe/channel profile, it does not extend beyond this point into the free stream. This accepts a small error compared to the actual value of the boundary layer edge velocity, $u_e/U \lesssim 1$ at $y/\delta_h = 1$, where U is the true free stream velocity reported with the data.

The procedure for determining δ_h for a given data set is illustrated in Figs. 17 and 18 using the $R_\tau = 1989$ DNS data of Sillero *et al.*[23] The dependence of the accuracy of the fit on the choice of u_e/U is shown in Fig. 17. The least error occurs for $u_e/U = 0.994$. If $u_e/U > 0.994$, the error increases rapidly because multiple points at the boundary layer edge are being used where the velocity is virtually constant. The optimization procedure will try to fit these points, and this will tend to degrade the fit over the rest of the profile increasing the error. If $u_e/U < 0.994$, the data are being cut off short of the boundary layer edge and the condition $du^+/dy^+ = 0$ at δ_h is being applied where the derivative is not quite zero, leading to a more gentle increase in the error. Figure 18 shows the dependence of R_τ on the choice of u_e/U. This is, in effect, the dependence of δ_h on u_e/U. The value $R_\tau = 1989$ reported with the data corresponds to $u_e/U = 0.990$. The new value of R_τ used to fit the universal velocity profile to the data is $R_\tau = 2088.5$.

The effects of these choices on the fit of the universal velocity profile to the Sillero *et al.*[23] data are shown in Figs. 19 and 20. The impact is, as expected, mainly in the outer flow where the universal profile comes in a bit too high or somewhat too low compared to the data. Figures 21 and 22 show the profile with the lowest error in linear and log coordinates. Figure 23 shows the log-indicator function for the lowest error case which is a particularly sensitive way to identify

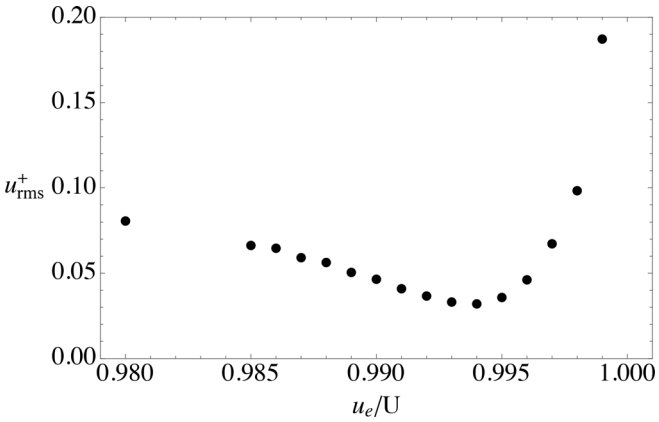

FIG. 17. Root-mean square error in u^+ between the DNS data of Sillero *et al.*[23] at $R_\tau = 1989$ and the universal velocity profile. Minimum error is achieved for δ_h chosen to be at $u_e/U = 0.994$.

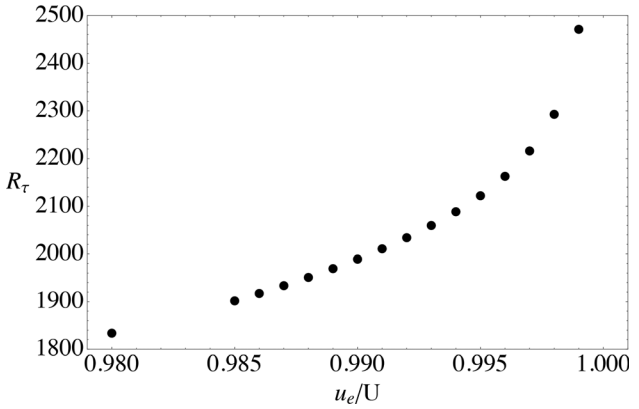

FIG. 18. Variation of R_τ with the choice of u_e/U. With δ_h chosen to be at $u_e/U = 0.994$, $R_\tau = 2088.5$, about 10% larger than the value $R_\tau = 1989$ at $u_e/U = 0.990$.

differences between the universal velocity profile and the data. The accuracy of the fit is excellent with $u^+_{rms} = 0.032$, on the order of 0.1%, compared to $u^+_{rms} = 0.047$ for $u_e/U = 0.990$. The optimal parameter values that achieve this accuracy are $(k, a, m, b, n) = (0.4289, 25.9290, 1.1480, 0.1696, 2.2516)$ compared to $(k, a, m, b, n) = (0.4187, 24.9525, 1.1982, 0.1760, 2.3713)$ for $u_e/U = 0.990$ from Subrahmanyam *et al.*[2] Due to the relatively low Reynolds number of the simulation, there is no significant logarithmic region of the profile in Fig. 23. The parameter values used to construct the integral boundary layer properties throughout this paper are those listed in Table I that are averaged over seven ZPG boundary layer simulations.[2]

VI. FRICTION LAW COMPARISONS

Recently,[4] the skin friction was measured on a flat plate in the range $10\,000 < R_{\delta_2} < 70\,000$ using an innovative thin oil-film interferometry method. They presented their data along with selected older data and with a variety of widely used classical friction laws from various authors which they corrected to a common set of experimental

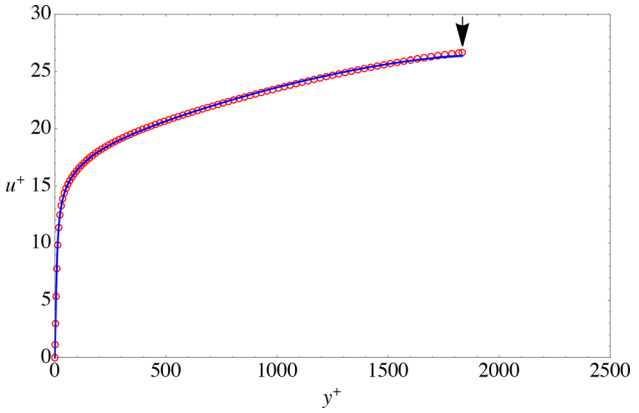

FIG. 19. Data from Sillero *et al.*[23] (open red discs) compared with the universal velocity profile with $u_e/U = 0.980$. The arrow indicates the error at the boundary layer outer edge where the blue solid line is too low.

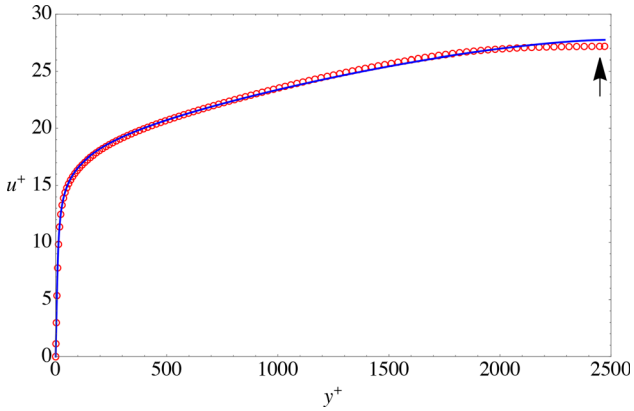

FIG. 20. Data from Sillero *et al.*[23] (open red discs) compared with the universal velocity profile with $u_e/U = 0.999$. The arrow indicates the error at the boundary layer outer edge where the blue solid line is too high.

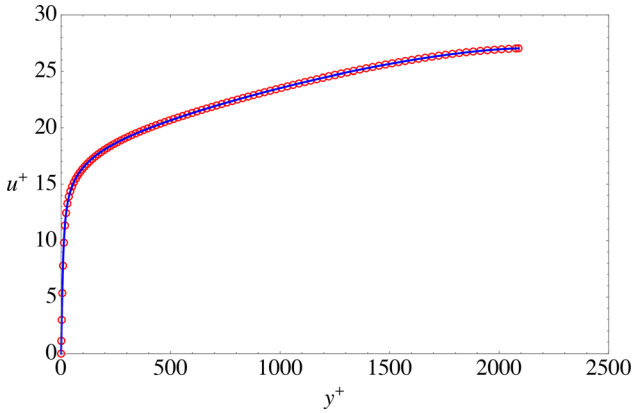

FIG. 21. Data from Sillero *et al.*[23] (open red discs) compared with the minimum error universal velocity profile with $u_e/U = 0.994$.

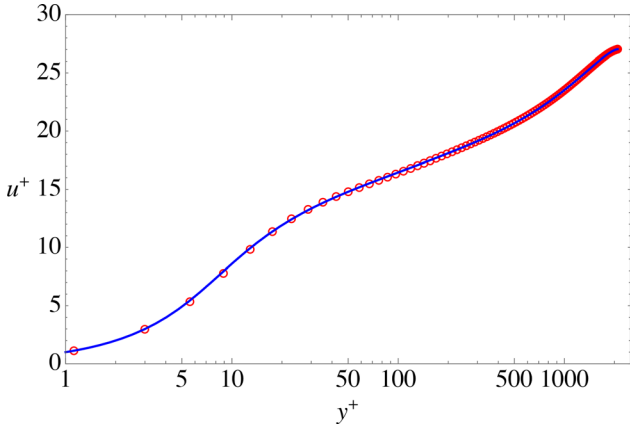

FIG. 22. Data from Sillero *et al.*[23] (open red discs) compared with the minimum error universal velocity profile with $u_e/U = 0.994$ in log-linear coordinates.

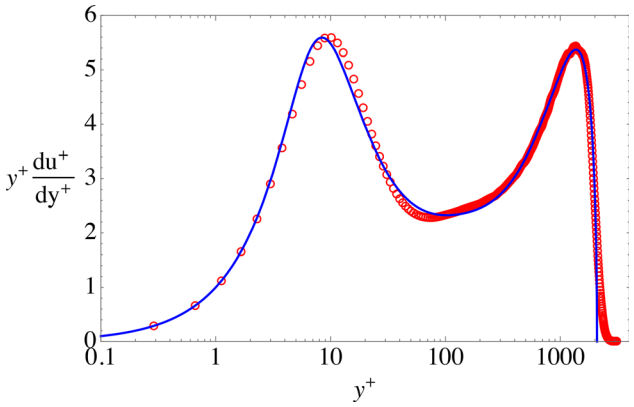

FIG. 23. Log indicator function with data from Sillero *et al.*[23] (open red discs) compared with the minimum error universal velocity profile with $u_e/U = 0.994$.

data. Figure 24 shows the friction coefficient generated by the universal velocity profile overlaid on their collected data in the Reynolds number range of their experiments. The agreement is quite good. They also used the collected data/friction laws to extrapolate the friction coefficient out to $R_{\delta_2} = 10^8$. Figure 25 shows their extrapolation compared to the friction coefficient generated by the universal velocity profile. Again, the agreement is quite good although the value of $C_f = 2(u_\tau/u_e)^2$ predicted by the universal velocity profile is slightly higher than the extrapolation in their Fig. 9. For example at $R_{\delta_2} = 10^8$, the universal velocity profile predicts $C_f = 0.00081$ compared to the range $0.00069 < C_f < 0.00076$ in Nagib *et al.*[4] While the disparity is quite small, it could indicate a possible weak dependence of the boundary layer velocity profile parameters on the Reynolds number.

VII. EVOLUTION OF THE BOUNDARY LAYER IN SPACE

The function $R_\tau = F_6(R_x)$, Eq. (54), generated by integrating Eq. (47), is shown in Fig. 14. The inverse function is shown in Fig. 13. Once F_6 is generated from the universal velocity profile, the rest of the spatial behavior of the boundary layer is easily produced. Figures 26–29 depict the stream-wise evolution of all the integral measures of the spatially developing boundary layer. The spatial friction law is presented in Fig. 30.

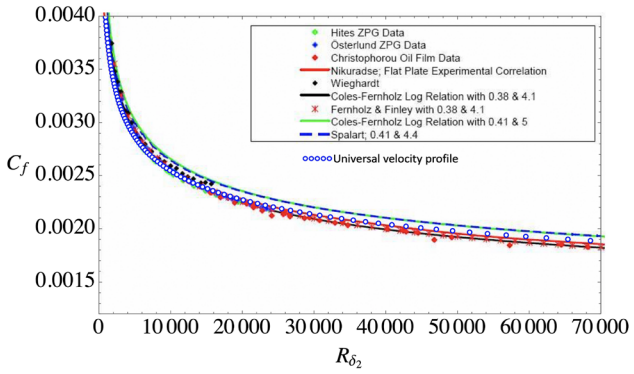

FIG. 24. Friction coefficient determined from (38) and (42) overlaid on Fig. 7 from.[4] Blue circles are generated from the universal velocity profile.

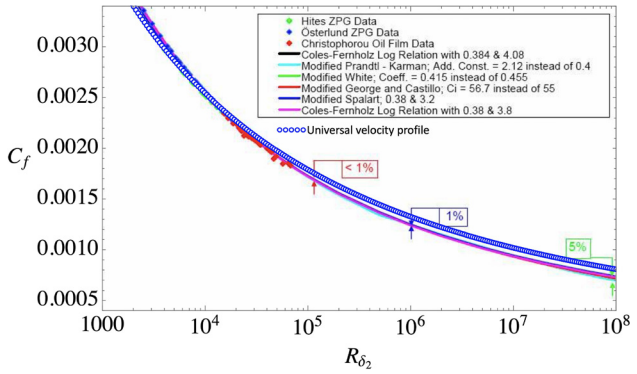

FIG. 25. Friction coefficient determined from (38) and (42) overlaid on Fig. 9 from.[4] Blue circles are generated from the universal velocity profile.

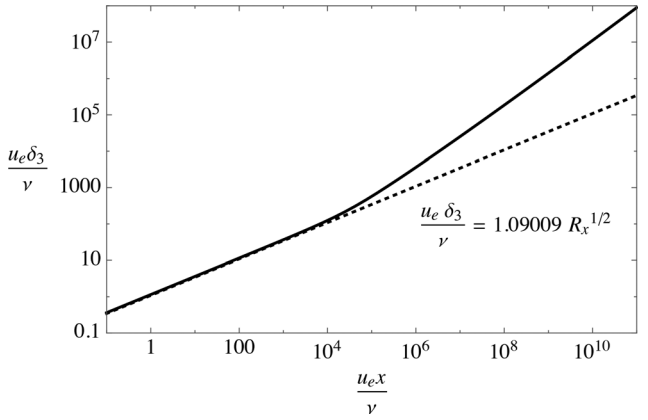

FIG. 28. Spatial evolution of the energy thickness Reynolds number.

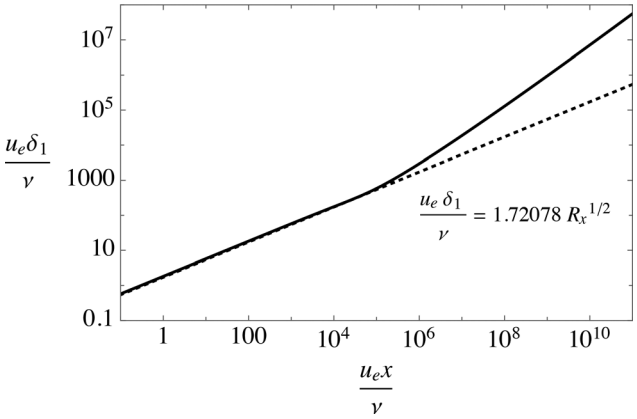

FIG. 26. Spatial evolution of the displacement thickness Reynolds number.

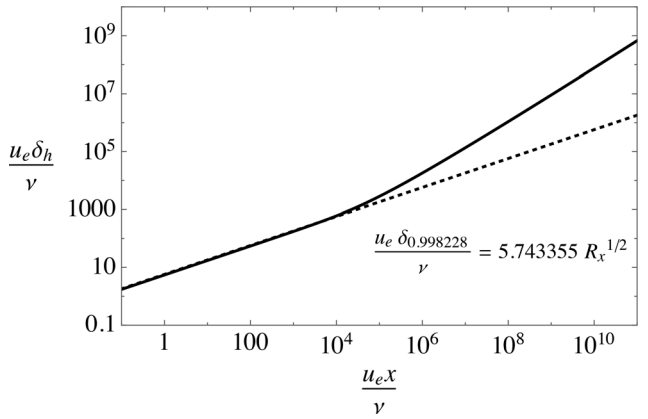

FIG. 29. Spatial evolution of the equivalent channel half height Reynolds number.

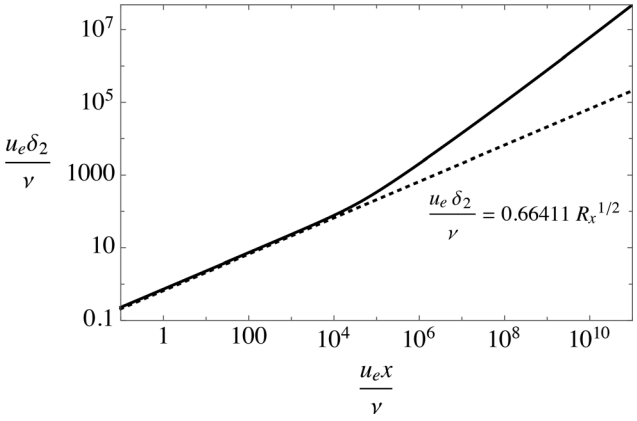

FIG. 27. Spatial evolution of the momentum thickness Reynolds number.

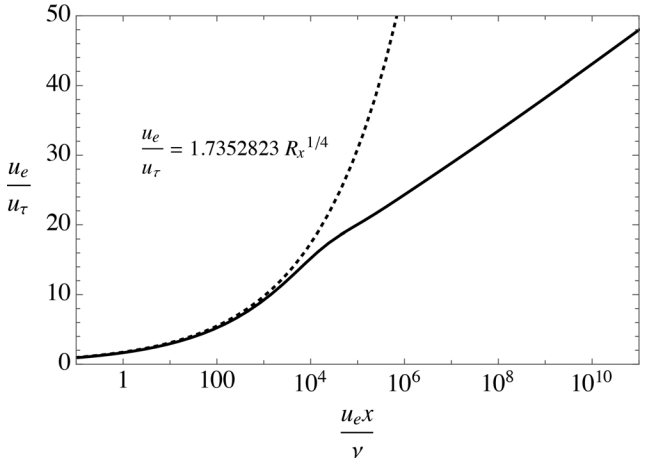

FIG. 30. Spatial evolution of the flat plate zero pressure gradient friction law.

The evolution of a turbulent boundary layer is often characterized by power law behavior. According to Eq. (53), to a leading order at extreme Reynolds numbers, $R_x \approx \ln(R_\tau)^2 R_\tau$. This nearly linear relation between R_x and R_τ explains why Figs. 26–29 all display nearly straight line, i.e., almost power-law, behavior at large values of R_x. However, the curves in Figs. 26–29 really cannot be approximated by a power law except by choosing a narrow range of Reynolds number and changing the power law exponent when the range changes. In actuality, there is no need for a power-law fit when $R_\tau = F_6(R_x)$ is a known function.

The spatial friction law generated using (38) and $F_6(R_x)$ is presented in Fig. 30. Given the position x, free stream speed, u_e, and kinematic viscosity ν, the friction velocity, u_τ, is immediately determined.

VIII. CONCLUSION

The universal velocity profile developed originally for pipe flow[1] has recently been shown to provide a very accurate approximation to channel flow and boundary layer flow with zero and adverse pressure gradient.[2,3] The profile is uniformly valid over the entire range, $0 \le y \le \delta_h$ and $0 \le R_\tau < \infty$. Choosing the boundary layer thickness that minimizes the error between velocity profile data and the universal profile defines, in a practical sense, an overall boundary layer thickness, δ_h, thereby avoiding the usual ambiguity in the identification of the boundary layer edge. The calculations presented here as solid lines in Figs. 6–15 and 26–30 are generated by integrating the universal velocity profile from $R_\tau = 0$, in other words, from the plate leading edge. In the low Reynolds number limit, the universal velocity profile approaches the laminar channel/pipe flow shape. The Blasius solution with a thickness corresponding to $u/u_e = 0.998228$ is provided for comparison in all the figures. This choice matches the channel and Blasius friction Reynolds numbers, $R_{\tau_{channel}} = R_{\tau_{Blasius}}$, while accepting about a 10% higher wall shear stress in the laminar part of the flow. These calculations also use the transition from laminar to turbulent flow inherent in the universal velocity profile. There is no particular need to do this, and an alternative approach that matches the Blasius profile, followed by a preferred transition model to the turbulent universal velocity profile, is an option.

At Reynolds numbers, $kR_\tau > 2000$, the universal velocity profile defines a Reynolds number independent shape function discussed in Sec. III and shown in Figs. 4 and 5. Figure 5 can be thought of as a cut through Fig. 4 at some large value of R_τ greater than about 5000. Equation (26) enables the high Reynolds number limiting behavior of all the integral measures of the boundary layer, as well as the skin friction law to be determined as functions of R_τ and as functions of R_x. The various limiting functions, Eqs. (27), (40), (43), (45), (49), and (53), are all shown as dashed lines in the appropriate figure. These figures confirm the rapid approach with the Reynolds number of the full integration of the universal velocity profile (solid line) to the high Reynolds number limit (dashed line). The prevalence of terms involving $\ln(R_\tau)$ in these limits accounts for why the flow changes so slowly at extreme Reynolds numbers.

Cantwell[1] conjectured that the functional form of the velocity profile given in (26) and (28) holds in the limit of infinite Reynolds number for pipe flow. This conjecture is extended here to include the boundary layer on a flat plate.

ACKNOWLEDGMENTS

I would like to express appreciation to Stanford University for continued support. I especially thank the referees for carefully reading the paper and providing helpful comments and suggestions. Thanks also to Joe Majdalani and PoF Editor-in-Chief, A. Jeffrey Giacomin for organizing this special issue. This paper is dedicated to Frank M. White on the occasion of his 88th birthday and in recognition of his classic textbook that has helped teach fluid mechanics to generations of engineering students around the world.

DATA AVAILABILITY

All data presented in the paper can be generated from the universal velocity profile or the solution of the Blasius equation.

REFERENCES

[1]B. J. Cantwell, "A universal velocity profile for smooth wall pipe flow," J. Fluid Mech. **878**, 834–874 (2019).
[2]M. A. Subrahmanyam, B. J. Cantwell, and J. J. Alonso, "A universal velocity profile for turbulent wall flows," AIAA Paper No. 2021-0061, 2021.
[3]M. A. Subrahmanyam, B. J. Cantwell, and J. J. Alonso, "A universal velocity profile for turbulent wall flows including adverse pressure gradient boundary layers," J. Fluid Mech. (unpublished) (2021).
[4]H. Nagib, C. Christophorou, J. Reudi, P. Monkewitz, J. Osterlund, and S. Gravante, "Can we ever rely on results from wall-bounded turbulent flows without direct measurements of wall shear stress?," AIAA Paper No. 2004-2392, 2004.
[5]T. von Kármán, "Uber laminaire und turbulente reibung," Z. Angew. Math. Mech. **1**, 233–252 (1921).
[6]L. Prandtl, "The mechanics of viscous fluids," in *Aerodynamic Theory*, edited by W. F. Durand (Springer, 1934), Vol. III, pp. 80–90.
[7]K. Pohlhausen, "Zur naherungsweisen integration der differentialgleichungen der laminaren reilbungsschicht," Z. Angew. Math. Mech. **1**, 252–260 (1921).
[8]B. Thwaites, *Incompressible Aerodynamics* (Oxford University Press, 1960), pp. 62–64.
[9]M. R. Head, *Entrainment in the Turbulent Boundary Layer* (Aeronautical Research Council, 1960), Vol. 3152.
[10]H. Ludweig and W. Tillman, *Investigations of Wall Shearing Stress in Turbulent Boundary Layers* (NACA TM, 1950), Vol. 1285.
[11]T. von Kármán, *Mechanical Similitude and Turbulence* (NACA TM, 1931), Vol. 611, pp. 1–21.
[12]L. Prandtl, "The mechanics of viscous fluids," in *Aerodynamic Theory*, edited by W. F. Durand (Springer, 1934), Vol. III, pp. 102–112.
[13]E. R. van Driest, "On turbulent flow near a wall," J. Aeronaut. Sci. **23**, 1007–1011 (1956).
[14]W. Kollmann, "Asymptotic properties of mixing length closures for turbulent pipe flow," Phys. Fluids **32**, 115126 (2020).
[15]D. I. Pullin, M. Inoue, and N. Saito, "On the asymptotic state of high Reynolds number, smooth-wall turbulent flows," Phys. Fluids **25**, 015116 (2013).
[16]S. Kawai and J. Larsson, "Wall-modeling in large eddy simulation: Length scales, grid resolution, and accuracy," Phys. Fluids **24**, 015105 (2012).
[17]S. Cai and P. Sagaut, "Explicit wall models for large eddy simulation," Phys. Fluids **33**, 041703 (2021).
[18]A. E. Perry and I. Marusic, "A wall-wake model for the turbulence structure of boundary layers. Part 2. Further experimental support," J. Fluid Mech. **298**, 361–407 (1995).
[19]M. V. Zagarola and A. J. Smits, "Mean-flow scaling of turbulent pipe flow," J. Fluid Mech. **373**, 33–79 (1998).
[20]B. J. Cantwell, *Introduction to Symmetry Analysis* (Cambridge University Press, 2002).
[21]F. M. White, *Fluid Mechanics*, 7th ed. (McGraw-Hill, 2011) pp. 461–471.
[22]J. Majdalani and L. Xuan, "On the Kármán momentum-integral approach and the Pohlhausen paradox," Phys. Fluids **32**, 123605 (2020).
[23]J. A. Sillero, J. Jiménez, and R. D. Moser, "One-point statistics for turbulent wall-bounded flows at Reynolds numbers up to $\delta^+ = 2000$," Phys. Fluids **25**, 105102 (2013).